How to cite: *Angew. Chem. Int. Ed.* **2025**, *64*, e202419550
doi.org/10.1002/anie.202419550

Electrosynthesis

Interfacial Asymmetrically Coordinated Zn–MOF for High-Efficiency Electrosynthetic Oxime

*Jiawei Kang[+], Peisen Liao[+], Runan Xiang, Wenpei Liao, Chenyu Yang, Shihan Wang, Qinghua Liu, and Guangqin Li**

Abstract: Oximes are important intermediates for various chemicals synthesis such as pharmaceuticals, among which one vital precursor for producing neurological disease, antimicrobial and anticancer agents is piperidone oxime (PDO). Compared with conventional thermocatalytic method, it's more attractive to synthesize PDO via green electrocatalytic technology especially utilizing waste nitrogen oxides gas as nitrogen source. However, there are great challenges in catalyst design for high-efficiency electrosynthetic oxime due to the low electron transport rate and multiple competing reactions. Herein, we propose an interfacial coordination strategy based on metal–organic frameworks (MOF) electrocatalyst for the first time to promote oxime electrosynthesis, by building Zn–O bridges between graphite felt (GF) and zeolitic imidazolate framework (ZIF-7/CGF). Specially, ZIF-7/CGF delivers a Faraday efficiency (FE) of 75.9 % with yield up to 73.1 % for 1-methyl-4-piperidone oxime, which is far superior to the catalyst without Zn–O bridges (a FE of 10.7 % and yield of 10.3 %). In-depth mechanism study shows that the introducing Zn–O bridges can promote the electron transfer and induce Zn sites transforming into distorted tetrahedron ($Zn\text{-}N_3O$) coordination mode, which benefits for intermediates adsorption and conversion. The developed strategy presents wide universalities towards various oximes electrosynthesis and adapts to other MOF materials (ZIF-8, ZIF-4). This work provides new insights for electrosynthetic organic chemicals and upgrading nitrogen cycle through rational design surficial coordinated electrocatalysts.

[*] J. Kang,[+] P. Liao,[+] R. Xiang, W. Liao, S. Wang, Prof. G. Li
Key Laboratory of Bioinorganic and Synthetic Chemistry of Ministry of Education, LIFM, IGCME,
School of Chemistry, Sun Yat-Sen University
Guangzhou 510006, China
E-mail: liguangqin@mail.sysu.edu.cn

C. Yang, Q. Liu
National Synchrotron Radiation Laboratory
University of Science and Technology of China
Hefei 230029, China

[+] These authors contributed equally to this work.

Introduction

Oximes are extensively applied in the synthesis of various drugs as important pharmaceutical precursors, exhibiting remarkable prospects in many fields.[1] Specifically, piperidone oxime (PDO) is a key precursor for Wnt/β-catenin signaling modulators, where the Wnt/β-catenin signaling pathway plays a vital role in maintaining tissue homeostasis by regulating the expression of target genes.[2] Additionally, PDO serves as an essential precursor for synthesizing the serotonin sub-type 6 ($5\text{-}HT_6$) modulators, which have been conducted in the preclinical studies for the treatment of neuropathological disorders, such as Alzheimer's disease and depression.[3] Furthermore, PDO is utilized in the synthesis and development of potent antimicrobial agents and Ribosomal S6 Kinase (RSK) inhibitors studied as potential anticancer agents.[4] Generally, PDO is mainly synthesized by the coupling reaction between piperidones (PD) and the strong nucleophilic reagent hydroxylamine (NH_2OH) through conventional thermal methods, which involves the storage, transportation and utilization of NH_2OH, increasing huge energy consumption and insecurity due to its instability and corrosiveness.[5]

On the other hand, nitrogen oxides (NO_x) pollution are mainly emissions from transportation and fuel combustion,[6] among which the paramagnetic molecule nitric oxide (NO) is the main component, causing marked excitation for humans by oxygen displacement, such as respiratory depression, lung injury and brain damage.[7] Furthermore, they can react with oxygen and water vapor to form nitrate particles and acidic aerosols, promoting the formation of acid rain, then leading to water eutrophication, and drastically reducing the agricultural crop yields as well.[8] N-containing organic molecules play important roles in lives, and practical synthesis of valuable N-containing organic compounds directly from N_2 or NO_x is of great significance in chemistry and chemical industry.[9]

Encouragingly, electrochemical NO_x reduction reaction (eNO_xRR) has a considerable insight in converting NO_x into NH_2OH and NH_3.[10] And the in situ production of NH_2OH from eNO_xRR has been utilized directly for synthesizing oximes by coupling carbonyl carbon source,[11] which is economical, energy-saving, environmental friendly and in line with the actual application scenario.[12] For example, cyclohexanone oxime prepared by electrosynthesis method from NO_x was achieved over carbon paper,[13] Fe nanoparticles,[14] Cu–S[15] or Cu/TiO_2,[16] and our group have developed self-standing carbon nanofiber membranes with

unsaturated Al–O and Fe–N sites for electrosynthesizing pyridine oximes and amino acids from NO_x.[17] However, there still exists big challenges in efficient catalysts design. Moreover, based on the experimental and theoretical calculation, NO is the key intermediate specie for electroreduction of nitrate and nitrite.[18] The most critical steps are the effective interfacial electron transport and proper adsorption energy of intermediates on the surfaces of electrode, but lack of effective methods to regulate the coordinated environment of catalytic sites achieving high-efficiency production of oximes in such a complex electrocatalytic system. The low solubility of NO in water (e.g., NO: 2 mM at ambient conditions)[19] makes it hard to compete with abundant water molecules, proton or hydroxide for water splitting.

Considering the facile adjustment of NO adsorption ability on catalytic sites and the mass transfer of substrate molecules, metal–organic frameworks with coordination bonds and high porosity are ideal platforms to investigate the relationship between structure and activity at the atom level, and powerful tools to adjust the adsorption strength of intermediate with coordinated regulation effect,[20] presenting great potential in biomimetic catalysis with high selectivity.[21] For example, ZIF-7, also well known as MAF-3, consists of Zn ions tetrahedral coordinated to benzimidazolate linkers, showing thermal and chemical stability, which has been widely applied in the field of energy conversion.[22] Zn ion also plays an important role in the production and transformation of messenger molecule NO, which is closely related to the central nervous and immune system.[23] Thus, ZIF-7 may have the potential performance for electrosynthetic oxime from NO. Although original MOF based catalyst has not been reported for NO reduction electrocatalysis, it exhibits great potential in this field because of its absorption ability advantages.[24]

Herein, we present an interfacial coordination regulation strategy to adjust the electronic state of ZIF-7 via Zn–O bridges over carboxylate graphite felt electrode interface by an in situ hydrothermal growth method. The mechanism investigation demonstrates the Zn–O bridges change the original tetrahedral configuration of zinc coordination mode, making the Zn sites adaptive for intermediates adsorption and activation. The electron transport was further augmented, thus achieving a high Faraday efficiency (FE) of 75.9 % and yield of 73.1 % for 1-methyl-4-piperidinone oxime (1-PDO) electrosynthesis. The output of high yield oxime 118.5 mg h^{-1} can be achieved in the scaled-up experiment. This work provides an innovative method for facilitating electron transport by constructing bridges between substrates and electrocatalysts and enriches the intermediate molecules adsorption by asymmetric coordination mode, which highlighted the huge application potential of eNO_xRR system for reusing natural resources in nitrogen cycle with the guidance of coordination chemistry.

Results and Discussion

As shown in Figure 1a, the graphite felt (GF) was carboxylated in the presence of nitric acid solution at 120 °C, and the appearance of C=O stretching vibration at 1726 cm^{-1} and asymmetric stretching of C–O at 1384 cm^{-1} from –COOH in the Fourier transform infrared spectroscopy (FT-IR) confirmed the successful carboxylation of GF,[25] donated as CGF (Figure S1). Subsequently, the CGF was immersed in the $Zn(NO_3)_2$ and benzimidazole solution for in situ growing ZIF-7 on the surface of modified GF through a solvothermal method, the final material named as ZIF-7/CGF. For comparison, ZIF-7 was also in situ growing on the surface of GF in the similar way, named ZIF-7/GF. Powder X-ray diffractometry (PXRD) was first used to characterize the phase composition of ZIF-7/CGF and ZIF-7/GF, clear characteristic peaks of ZIF-7 crystals and graphite carbon were observed in both of two samples (Figure S2). Meanwhile in the FT-IR spectrum of ZIF-7/CGF, a new bond assigned to Zn–O vibrational bands appeared at 420 cm^{-1}, indicating the formation of coordinated bonds between Zn^{2+} and carboxyl group of CGF.[26] In contrast, the Zn–O bond was not found in ZIF-7/GF (Figure S3). Scanning electron microscope (SEM) and transmission electron microscope (TEM) were further carried out to observe the microstructure of samples. Compared with CGF (Figure S4), a number of regular particles around 250–300 nm in size appeared and homogeneously dispersed on the nanofibers with an average size of 20 μm (Figure 1b). While for ZIF-7/GF, smaller particles around 150–200 nm scattered across the nanofibers (Figure S5), which may be caused by the lack of anchoring sites on GF. Aberration-corrected high-angle annular dark-field scanning transmission electron microscopy (HAADF-STEM) and energy dispersion X-ray spectroscopy (EDX) mappings (Figure 1c, Figure S6 and Figure S7) demonstrated the Zn, O, C and N elements were uniformly distributed in the structure of ZIF-7/CGF. Raman spectra was further employed to characterize the structure of samples. The D-band around 1360 cm^{-1} and G-band around 1580 cm^{-1} were ascribed to the disordered carbon and relative motion of sp^2 carbon, respectively. I_D/I_G (intensity ratio of the two bands) was usually recognized as an indicator to evaluate the carbon defect in carbon materials.[27] As showed in Figure S8, the ratio of I_D/I_G for CGF (0.99) was similar to GF (1.01), indicating carboxylation did not affect the degree of graphitization much. Nevertheless, both ZIF-7/GF (0.92) and ZIF-7/CGF (0.87) showed a decrease of carbon defects, further confirming the introduction of ZIF-7 sp^2 carbon framework. Next, the porosity changes from CGF to ZIF-7/CGF were explored with the assistance of N_2 physisorption experiments at 77 K. As shown in Figure S9 and Table S1, compared with CGF, the adsorption capacity of ZIF-7/CGF decreased significantly, which was considered as causing by the introduction of ZIF-7 with ultra-micropore on the surface of CGF, blocking the entry of nitrogen molecules. Thus, the structure of ZIF-7/CGF with ZIF-7 in situ growing on the surface of carboxyl graphite felt through Zn–O coordinated bridge was confirmed. The Zn content in ZIF-7/CGF based on

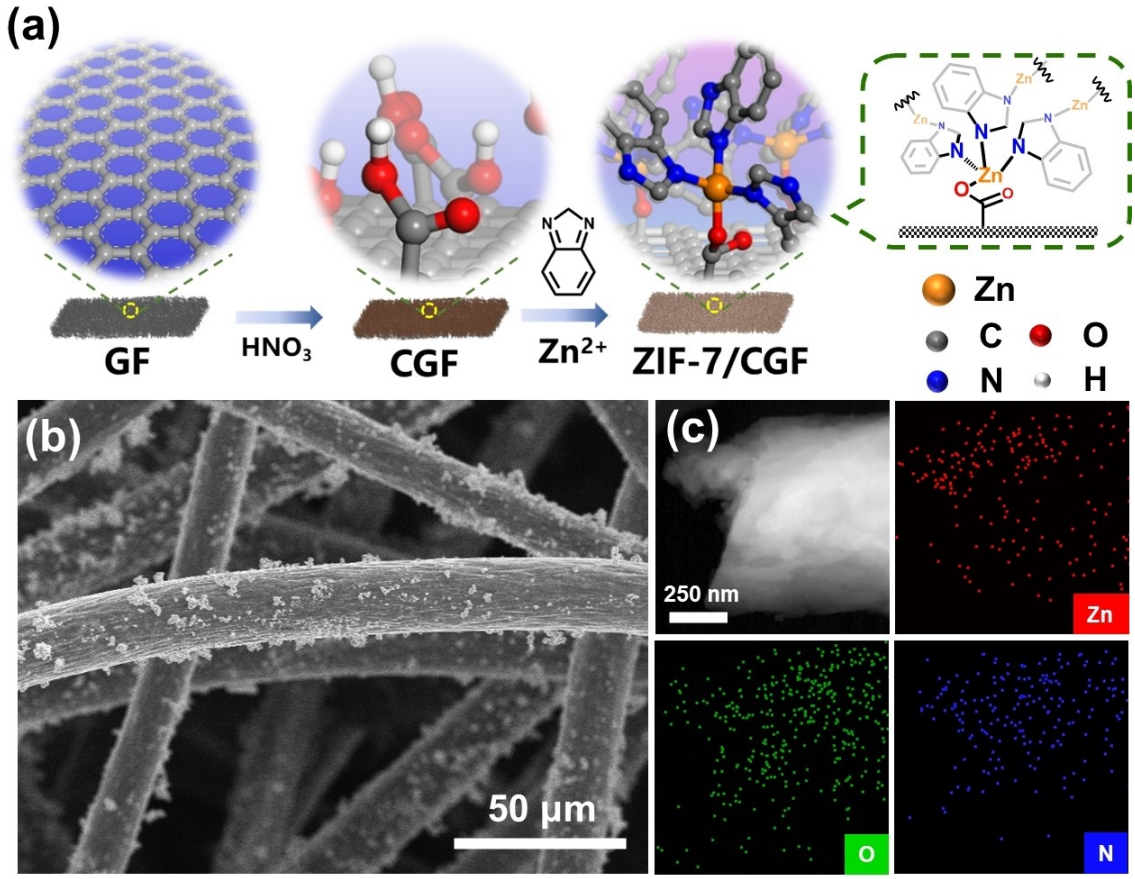

Figure 1. Synthesis and morphology characterizations of ZIF-7/CGF. (a) Schematic illustration of synthetic ZIF-7/CGF; (b) SEM, (c) HAADF-STEM images of ZIF-7/CGF with corresponding EDX mappings of O, N and Zn elements.

Inductively coupled plasma-atomic emission spectroscopy (ICP-AES) was about 0.56 % (Table S2).

X-ray photoelectron spectroscopy (XPS) and X-ray absorption fine structure (XAFS) were employed to investigate the chemical state and surface environment of ZIF-7/CGF and ZIF-7/GF (Figure S10–S11). The Zn 2*p* high-resolution spectra of ZIF-7/GF displayed a peak at 1022.52 eV for Zn $2p_{3/2}$ corresponding to the Zn species of ZIF-7. For ZIF-7/CGF, a new peak located at 1024.22 eV was referred to Zn–O species originated from the coordination of Zn in MOF with carboxyl groups in CGF. Furthermore, compared to ZIF-7/GF, a slightly negative shift of Zn-N_4 in ZIF-7/CGF (0.26 eV) was observed, suggesting a decreased oxidation state of Zn in ZIF-7 and charge transfer from ZIF-7 to the Zn–O surface (Figure 2a). To gain a deeper understanding the structure of ZIF-7/CGF, the measurement of X-ray absorption spectroscopy (XAS) was performed. As seen from the X-ray absorption near-edge structure (XANES) spectra of Zn *K*-edge (Figure 2b), it could be implied that Zn of ZIF-7/CGF and ZIF-7/GF showed a similar oxidation state closed to ZnO and ZIF-7, and the edge position of ZIF-7/CGF was slightly shifted to higher energy, indicating that the average valence of Zn in ZIF-7/CGF was a little higher than that in ZIF-7/GF. The more electron-negative state of Zn in ZIF-7/CGF might enhance the adsorption of relatively electron-rich NO during the eNORR, thus promoting the efficiency of reaction. In addition, the corresponding Fourier transformed (FT) k^3-weighted extended X-ray absorption fine structure (EXAFS) was investigated to further reveal the local environment of Zn in ZIF-7/CGF. As seen in Figure 2c, the main peak of ZnO and ZIF-7 exhibited at 1.54 Å and 1.57 Å, attributed to the Zn–O and Zn–N bonds, respectively.[28] Interestingly, the main peak of ZIF-7/CGF showed a slightly shift downward, indicating a difference of coordination environment with ZIF-7. While the main peak of ZIF-7/GF was almost the same as ZIF-7, revealing a similar coordination to ZIF-7. The EXAFS fitting was carried out to deeply understand the Zn coordination environment. The EXAFS fitting curves were shown in Figure S12–S13, Figure 2d and Table S3. The as synthesized ZIF-7 and ZIF-7/GF were well fitted with the model of ZIF-7 crystal. As the average coordination number of local Zn atom in ZIF-7/CGF was about 4 (Figure 2d),[29] the carboxyl group existed on the surface of GF in carboxylation process, which was easily coordinated with Zn^{2+} during construction of ZIF-7/CGF. Furthermore, Zn–O bonds were found in the FT-IR and XPS results. Additionally, XRD results revealed the existence of Zn–N bonds attributed to the observation of the ZIF-7 phase, it was concluded that Zn–O and Zn–N coexist

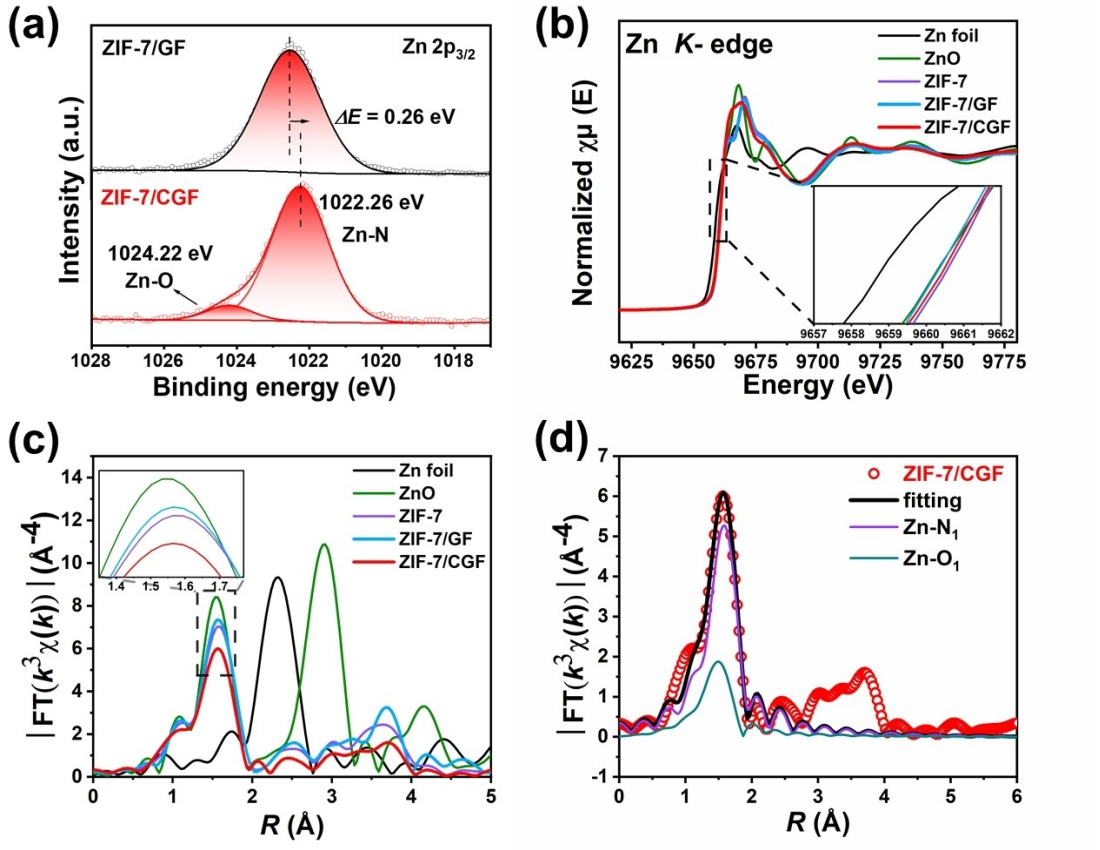

Figure 2. (a) Zn 2p spectra of ZIF-7/GF and ZIF-7/CGF; (b) XANES spectra of Zn *K*-edge of ZIF-7/CGF (red) and ZIF-7/GF (blue), referenced Zn foil, ZnO, ZIF-7; (c) Fourier-transformed (FT) k^3-weighted $\chi(k)$-function EXAFS spectra of the ZIF-7/CGF (red) and ZIF-7/GF (blue) and the references; (d) EXAFS fitting curves of ZIF-7/CGF in *R* space.

in ZIF-7/CGF. Based on density functional theory (DFT) calculation, the formation energy of Zn–N_3O on the surface is the lowest compared to other models (Figure S14). This implies that during the in situ growth of ZIF-7 on CGF, the Zn-N_3O coordination on the interface is favored.

Electrosynthesis of piperidone oximes. The electrocatalytic performance of ZIF-7/CGF for 1-PDO production was assessed in a 30 mL H-type cell containing 0.1 M KOH aqueous solution, where ZIF-7/CGF was used directly as working electrode for its self-standing property (Figure 3a). The linear sweep voltammetry (LSV, Figure 3b) showed that the current density was markedly enhanced in the NO atmosphere compared with that under argon (Ar) atmosphere, indicating the NORR is more favorable than HER and hydrogenation of 1-PD. When 1-PD was added into the electrolyte, leading to a decrease current density, which might reason from the catalytic sites was covered and solution conductivity declined. Then, chronopotentiometry was used to explore the electrochemical co-reduction activity of ZIF-7/CGF at the control potential of −0.1 V versus reversible hydrogen electrode (vs. RHE) for 2 h, and the electrolyte after electrocatalysis was analyzed and quantitated by ^{1}H nuclear magnetic resonance (^{1}H NMR, Figure S15–S16). The new appeared characteristic peaks at 2.14, 2.21, and 2.43 ppm in the ^{1}H NMR were in accordance with the commercial 1-PDO and the peaks of reactant (1-PD) decreased dramatically, demonstrating the successful conversion of 1-PD into 1-PDO via co-electroreduction of NO. Meanwhile, without entry of 1-PD, ammonia (NH_3) and NH_2OH were detected in the liquid phase based on Ultraviolet-visible (UV-Vis) spectrophotometry (Figure S17–S21). Furthermore, the ability of ZIF-7/CGF in electrosynthesizing 1-PDO under various potentials (0.1 V to −0.5 V vs. RHE) was tested. The FE of 1-PDO exceed 40 % across a wide range of voltages (0.1 to −0.1 V *vs.* RHE), giving a best FE of 53.4 % and yield of 70.5 % at −0.1 V vs. RHE (Figure S22–25). The concentration of 1-PDO was much superior to that of NH_2OH in the absence of 1-PD (Table S4–S5), suggesting the consumption of NH_2OH during the C–N coupling process results in the accelerated kinetics of NORR into NH_2OH. Compared with the stepwise synthesis, in situ utilization of the NH_2OH during NORR was more efficient and energy-saving.

To identify the nitrogen source of 1-PDO, the electrochemical synthesis proceeded under Ar atmosphere. No 1-PDO product was detected by ^{1}H NMR, implying that the electrocatalytic production of 1-PDO involved the participation of NO (Figure S26). Meanwhile, the system operated at

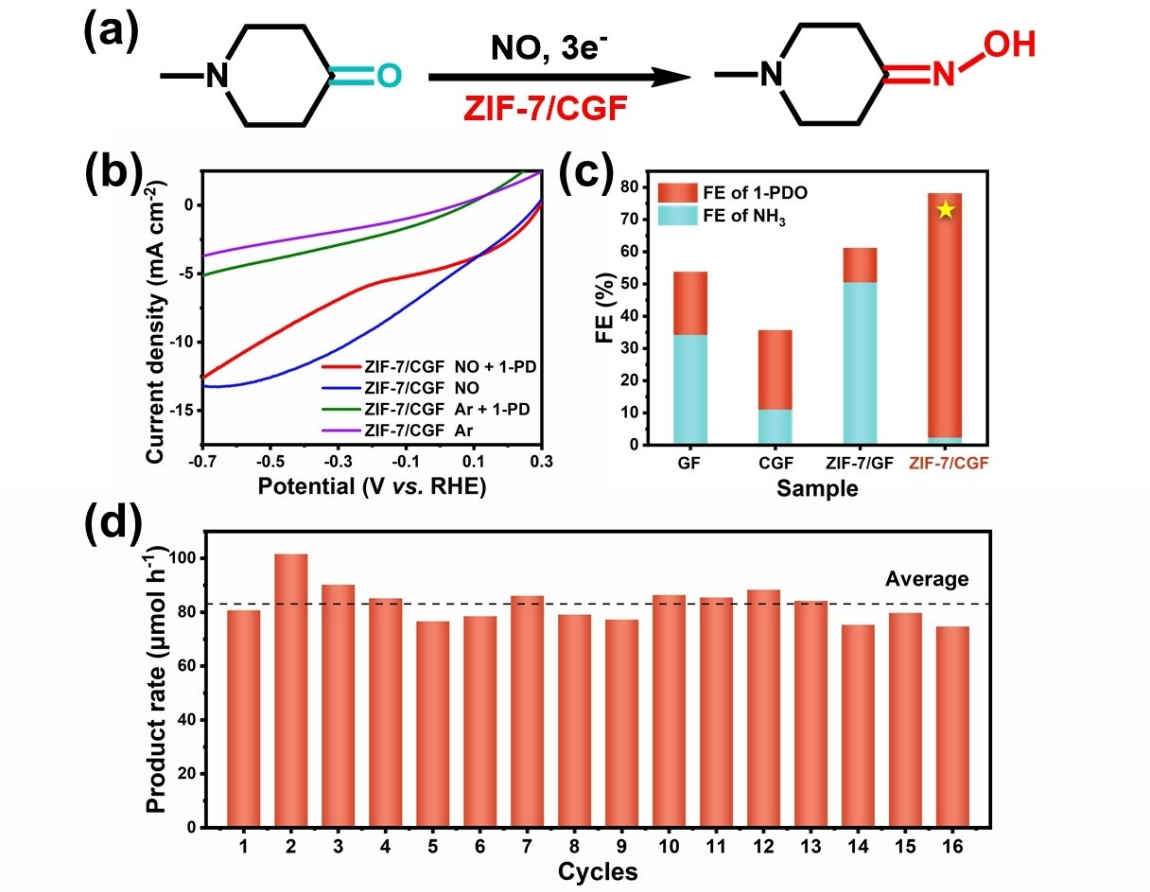

Figure 3. (a) The synthetic route for 1-PDO from 1-PD and NO driven by electricity over ZIF-7/CGF; (b) LSV curves of ZIF-7/CGF under various conditions; (c) The FE and yield of electrosynthesis 1-PDO and NH_3 over GF, CGF, ZIF-7/GF and ZIF-7/CGF; (d) The long-term stability test for 1-PDO production on ZIF-7/CGF.

open circuit voltage (OCV), there was no characteristic peak of 1-PDO observed in the ^{1}H NMR spectrum, revealing electricity was the essential driving force for the reaction (Figure S27). It was also found that the active hydrogen (*H) utilization played an important role in the reaction as the FE sharp declined when the free radical inhibitor tert-butanol was introduced to capture *H (Figure S28).

Then the electrocatalytic performance of various materials was evaluated to investigate the active sites in ZIF-7/CGF (Figure 3c, Figure S29–S32 and Table S6) based on chronoamperometry at 12 mA, which allowed the electrolysis reaction evenly.[30] Compared to uncarboxylated GF (a FE of 19.6 %), CGF had a slightly higher FE (24.7 %) at the same condition, which might be attributed to the enhancement of NO chemisorption ability from carbonyl group.[31] It has been observed that NH_3 is the predominant N-containing product on GF substrate, whereas on CGF substrate the primary product is oxime (Figure 3c, Figure S33). This disparity is further enhanced upon loading ZIF-7. The FE of 1-PDO on ZIF-7/CGF was significantly raised to 75.9 % with a yield up to 73.1 %, While for ZIF-7/GF, the FE was only 10.7 %. These results emphasized the importance of the establishment of Zn–O on the interface and the function of ZIF-7 in suppressing hydrogen evolution,[32] meanwhile enriching the water-insoluble NO molecules and 1-PD capture on the surface of electrode for accelerating the mass/electron transport. In addition, the differences in the electrocatalytic performance of the samples in situ adsorption of $Zn(NO_3)_2$ on GF and CGF named $Zn(NO_3)_2$/CGF and $Zn(NO_3)_2$/GF (a yield of 49.2 %, 11.5 % and FE of 51.2 %, 12.0 % for $Zn(NO_3)_2$/CGF and $Zn(NO_3)_2$/GF, respectively) further illustrated Zn were the reactive centers and the irreplaceable Zn–O bridges for electron transport (Figure S34–35, and Table S6). Furthermore, 1.0 M HCl was used to etch the framework of ZIF-7/CGF. As displayed in Figure S36 and Table S6, a sharp drop in productivity of 1-PDO (a yield of 35.6 % and FE of 37.0 %) was observed, implying the importance of MOF, which may help to inhibit HER and promote NO adsorption. The ZIF-7/CGF also showed high durability as the FE and production rates of 1-PDO maintained well even after 16 cycles (Figure 3d, Figure S37).

To further understand the evolution of local structure of Zn active sites and electrocatalytic NO_x co-reduction process in the corresponding working potentials, in situ XAFS measurements were carried out in a homemade reaction

cell. As seen in Figure 4a, compared with the condition in air, when potentials were applied, the intensities of white lines increased, which indicated the electron transition of Zn from 1 *s* to a 4*p*-orbital occupancy.[33] Additionally, a slightly low energy shift was observed in the edge position under the working conditions (Figure S38), suggesting an electrically driven reduction in valence state of Zn sites, which might be caused by the effective adsorption of the reactive species. Moreover, compared with the condition in air, the intensity of main peak for the electrocatalyst exhibited a significant increase in the supporting electrolytes under working conditions (Figure 4b), which was further speculated to the increased coordination number of Zn active sites due to the adsorption of substrate molecules driven by the electric field. In order to deeply clarify the electrocatalytic process over Zn sites at different applied potentials, the Zn *K*-edge EXAFS fitting at the first shell was performed, where a new Zn–N coordination was considered due to the interaction between Zn sites and nitrogen-containing active species in eNORR process and the results were shown in Figure 4c, Figure S39 and Table S7. Paramagnetic NO molecule could coordinate with Zn^{2+} ion,[34] which renders it highly reactive and difficult to high efficiently synthesize NH_2OH or oxime in the intermediate chemical valence states especially with the existence of active hydrogen atoms (Figure S28). Combined with the analysis of experimental results, the catalyst presented excellent oxime production performance at 0.1 V vs. RHE, demonstrating that the adsorption of NO reduction species tended to be saturated and reach a rapid adsorption and desorption state of the active intermediates to NH_2OH. Especially, the generation of key intermediate NH_2OH rapidly coupled with substrates, which further accelerated the production of NH_2OH, thus continuously promoting the reaction. As the potential kept decreasing to −0.3 V *vs.* RHE, the coordination number of Zn sites did not significantly change, which revealed the dynamic equilibrium of adsorption and desorption of intermediates on Zn sites still maintained even with the voltage widening. The coordination number decreased when the potential decreased to −0.5 V vs. RHE, which may reason from the competitive reactions (HER and NORR to NH_3) became the dominating processes and much rapider desorption of intermediates occurred under high potentials. The above XAFS fitting results and analysis were consistent with the experimental results, which clearly clarified the NO reduction took place efficiently at the Zn sites with sustainable activity. The potential-driven redistribution of electronic orbital during the electrosynthesis oximes process was well presented, highlighting the significant role of Zn–O interfacial active sites in ZIF-7/CGF. This process involves dynamic changes of the geometrical coordination structure across a wide potential range, resulting in highly oximes-producing activity within a multi-competition system.

To further identify the reaction pathway of NO_x reduction species coupling with 1-PD, in situ attenuated total refraction Fourier transform infrared spectrometer (ATR-FTIR) measurements under corresponding working potentials were performed (Figure 4d and 4e). As the

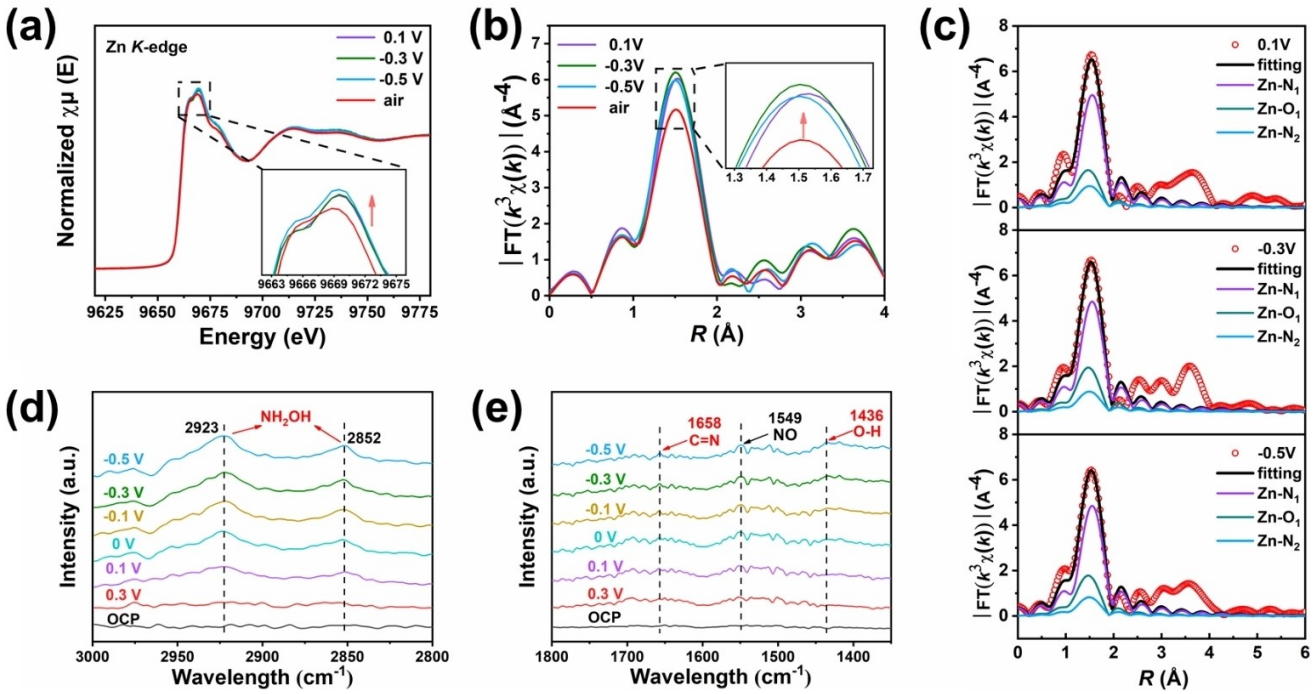

Figure 4. In situ XAFS and ATR-FTIR measurements. (a) In situ XANES spectra recorded at Zn *K*-edge of ZIF-7/CGF under air condition and different applied potentials from 0.1 to −0.5 V vs. RHE; (b) Corresponding k^3 at Zn *K*-edge under typical working conditions (air, 0.1, −0.3, −0.5 vs. RHE); (c) The fitting curves recorded at Zn *K*-edge under typical working conditions (0.1, −0.3, −0.5 vs. RHE); (d) and (e) ATR-FTIR spectra of ZIF-7/CGF carried out during electrosynthesis of 1-PDO from 0.3 to −0.5 V vs. RHE.

potential decreased from 0.3 to −0.5 V, the progressively increasing IR absorption bands were observed at 2923 cm^{-1} and 2852 cm^{-1} which were assigned to N–H bonds stretching vibration, indicating the key intermediates NH_2OH appeared and accumulated on the ZIF-7/CGF electrocatalyst (Figure 4d).[35] As shown in Figure 4e, the vibration bands at 1658 cm^{-1} and 1436 cm^{-1} were assigned the stretching vibration of C=N and the bending vibration of O–H of oxime, respectively. The peaks are consistent with the experimental ex situ FT-IR spectrum of standard 1-PDO and NH_2OH in 0.1 M KOH (Figure S40). The increase of absorption intensity with the increasing potential indicated that oximes were accumulated. To be noted that the appeared vibration bands at 1549 cm^{-1} were attributed to the bending vibration of NO.[35c,36] Combining the above results with experiments, the mechanism was confirmed as: NO was first adsorbed by ZIF-7/CGF, then the electrically driven reduction from NO to $*NH_2OH$ was occurred. Subsequently the $*NH_2OH$ was coupled with ketone substrates through nucleophilic reactions to form oximes. The formation Zn–O bridge boosted the interfacial electron transport and suppressed hydrogen evolution reaction to promote for generating key intermediates (*H and $*NH_2OH$), thereby leading to a high efficiency of oxime electrosynthesis.

To verify the universality of interfacial coordinated engineering strategy for enhancing the electrocatalytic conversion of NO coupling piperidone co-reduction into piperidone oximes, various Zn-based MOF (ZIF-4, ZIF-8) in situ growing on carboxylated and uncarboxylated graphite felt were prepared and their performances were displayed in Figure S41–S47 and Table S8. All of the catalysts with Zn–O bridges show a higher FE and production rate compared with the unmodified catalysts, indicating the broad universality of the developed method. In addition, other nitrogen sources (e.g., NO_2, NO_2^- and NO_3^-) also exhibited excellent performance in the electrocatalytic synthesis of 1-PDO, illustrated the potential of ZIF-7/CGF in electrochemical reduction of effluent containing NO_x species (Figure S48–S50, Table S9). Furthermore, as shown in the Figure S51–S55 and Table S10, the ZIF-7/CGF catalyst was also suitable for other ketone and aldehyde oximes synthesis, which were important intermediates for psychotherapeutic drugs, demonstrating the great potentials in the medicine molecular synthesis. The scale-up preparation of ZIF-7/CGF (area of 5×8 cm^2) was also easily operated (Figure S56 and Table S11), and the amplified catalyst also showed excellent catalytic performance, corresponding to a FE of 46.5 % and a 1-PDO production rate of 118.5 mg h^{-1}, manifesting the great application potential in NO conversion to oxime by electrosynthesis.

Conclusions

In summary, we have developed an interface coordination strategy to efficiently converse NO into highly value-added piperidone oximes through constructing Zn–O bridges between ZIF-7 and carboxylated graphite felt matrix. The obtained ZIF-7/CGF delivers a 1-PDO oximes FE of 75.9 % and yield of 73.1 %, which greatly enhanced comparing to ZIF-7/GF without Zn–O bridges. The impressive promotion in electrochemical conversion of NO into piperidone oximes originates from the self-adaptive Zn–O bridges and reconstruction of Zn coordinated environment on the surface from regular tetrahedron ($Zn–N_4$) to distorted tetrahedron ($Zn–N_3O$), the structure transformation brings open sites and electron-deficient state, which benefits for the adsorption and activation of intermediates. Meanwhile, Zn–O bridges over MOF and conductive graphite felt substrate can also accelerate the efficient electron transfer. Furthermore, this effective approach is universal for constructing other MOFs for enhancing the electrocatalytic efficiency of various oxime synthesis from nitrogen-containing exhaust gas and laden wastewater. Specially, the ZIF-7/CGF catalyst is easily magnified and operated to achieve a production rate of 118.5 mg h^{-1} for 1-PDO in the laboratory. This study shows the important potential of rational designing efficient catalysts through interface coordinated engineering for critical electrochemical conversion of harmful NO into valuable organonitrogen and fixing nitrogen cycle, also brings new insights between inorganic and organic chemistry, promoting the development of electrosynthesis.

Acknowledgements

This work was supported by the Overseas High-level Talents Plan of China, the NSFC Projects (22375223 and 22075321), the Program for Guangdong Introducing Innovative and Entrepreneurial Teams (2017ZT07C069) and Guangdong Basic Research Center of Excellence for Functional Molecular Engineering.

Conflict of Interest

The authors declare no conflict of interest.

Data Availability Statement

The data that support the findings of this study are available from the corresponding author upon reasonable request.

Keywords: Nitrogen oxides · Oximes · Metal–organic framework · Electrocatalysis · Electrosynthesis

[1] a) B. Li, J. Chen, D. Liu, I. D. Gridnev, W. Zhang, *Nat. Chem.* **2022**, *14*, 920–927; b) M. K. Mohan, K. Thorat, T. P. Puthiyapurayil, O. Sunnapu, S. Chandrashekharappa, V. Ravula, R. Khader, A. Sankaranarayanan, H. Muhammad, P. K. Vemula, *Nat. Commun.* **2024**, *15*, 4844; c) J. Mas-Roselló, T. Smejkal, N. Cramer, *Science* **2020**, *368*, 1098–1102; d) M. Fujita, G. M. Policastro, A. Burdick, H. T. Lam, J. L. Ungerleider, R. L. Braden, D. Huang, K. G. Osborn, J. H. Omens, M. M. Madani, K. L. Christman, *Nat. Commun.* **2021**, *12*, 3764.

[2] a) S. K. Kc, C. C. Mak, B. W. Eastman, J. T. Marakovits, V. Bollu, J. Cao, G. K. Mittapalli, World Intellectual Property Organization, WO2020150545 A1, **2020**; b) J. Liu, Q. Xiao, J. Xiao, C. Niu, Y. Li, X. Zhang, Z. Zhou, G. Shu, G. Yin, *Sig. Transduct. Target. Ther.* **2022**, *7*, 3.

[3] a) P. R. Guzzo, A. J. Henderson, M. Isherwood, C. Y. Lee, A. Ghosh, H. Zhao, World Intellectual Property Organization, WO2012099952 A2, **2012**; b) D. Karila, T. Freret, V. Bouet, M. Boulouard, P. Dallemagne, C. Rochais, *J. Med. Chem.* **2015**, *58*, 7901–7912.

[4] a) C. Ramalingan, Y. T. Park, S. Kabilan, *Eur. J. Med. Chem.* **2006**, *41*, 683–696; b) S. T. Harini, H. V. Kumar, S. K. Peethambar, J. Rangaswamy, N. Naik, *Med. Chem. Res.* **2014**, *23*, 1887–1898; c) S. E. Dunn, A. Jayanthan, J. R. Nagireddy, S. Annedi, J. H. Van Drie, T. S. Daynard, M.-M. Huynh, World Intellectual Property Organization, WO2017141116 A1, **2017**; d) Y. Sun, L. Tang, C. Wu, J. Wang, C. Wang, *Eur. J. Med. Chem.* **2023**, *251*, 115229; e) G. Jin, M. Yan, K. Liu, K. Yao, H. Chen, C. Zhang, Y. Yi, K. Reddy, D. R. Gorja, K. V. Laster, Z. Guo, Z. Dong, *Oncogene* **2020**, *39*, 6733–6746.

[5] a) S. Y. Han, J. W. Choi, J. Yang, C. H. Chae, J. Lee, H. Jung, K. Lee, J. D. Ha, H. R. Kim, S. Y. Cho, *Bioorg. Med. Chem. Lett.* **2012**, *22*, 2837–2842; b) P. Gross, *Crit. Rev. Toxicol.* **1985**, *14*, 87–99; c) S. C. Gad, In *Encyclopedia of Toxicology (Third Edition)* **2014**, *2*, 982–983.

[6] a) G. D. Thurston, *Inter. Encycl. Public Health* **2017**, *12*, 367–377; b) C. Lin, K. Kim, Z. Wang, Z. Yan, Z. Tang, Y. Liu, *Nano Res.* **2023**, *16*, 13366–13374.

[7] a) S. B. DuTeaux, In *Encyclopedia of Toxicology (Fourth Edition)* **2024**, *9*, 1–6; b) X. Chen, H. Wang, S. Du, M. Driess, Z. Mo, *Angew. Chem. Int. Ed.* **2022**, *61*, e202114598.

[8] a) G. D. Thurston, L. C. Chen, M. Campen, *Science* **2022**, *375*, 506–506; b) J. Peñuelas, J. Sardans, *Science* **2022**, *375*, 266–267; c) S. Shang, C. Yang, C. G. Wang, J. S. Qin, Y. Li, Q. F. Gu, J. Shang, *Angew. Chem. Int. Ed.* **2020**, *59*, 19680–19683.

[9] a) Z. J. Lv, J. Wei, W. X. Zhang, P. Chen, D. Deng, Z. J. Shi, Z. Xi, *Natl. Sci. Rev.* **2020**, *7*, 1564–1583; b) Q. Zhuo, J. Yang, X. Zhou, T. Shima, Y. Luo, Z. Hou, *J. Am. Chem. Soc.* **2023**, *145*, 22803–22813; c) Q. Zhuo, J. Yang, Z. Mo, X. Zhou, T. Shima, Y. Luo, Z. Hou, *J. Am. Chem. Soc.* **2022**, *144*, 6972–6980; d) X. Kong, J. Ni, Z. Song, Z. Yang, J. Zheng, Z. Xu, L. Qin, H. Li, Z. Geng, J. Zeng, *Nat. Sustain.* **2024**, *7*, 652–660; e) H. Jin, L. Li, X. Liu, C. Tang, W. Xu, S. Chen, L. Song, Y. Zheng, S. Z. Qiao, *Adv. Mater.* **2019**, *31*, e1902709; f) Y. Zhang, W. Qiu, Y. Ma, Y. Luo, Z. Tian, G. Cui, F. Xie, L. Chen, T. Li, X. Sun, *ACS Catal.* **2018**, *8*, 8540–8544; g) X. Fan, C. Liu, X. He, Z. Li, L. Yue, W. Zhao, J. Li, Y. Wang, T. Li, Y. Luo, D. Zheng, S. Sun, Q. Liu, L. Li, W. Chu, F. Gong, B. Tang, Y. Yao, X. Sun, *Adv. Mater.* **2024**, *36*, 240122.

[10] a) R. Hao, L. Tian, C. Wang, L. Wang, Y. Liu, G. Wang, W. Li, G. A. Ozin, *Chem Catalysis* **2022**, *2*, 622–638; b) J. Shao, H. Jing, P. Wei, X. Fu, L. Pang, Y. Song, K. Ye, M. Li, L. Jiang, J. Ma, R. Li, R. Si, Z. Peng, G. Wang, J. Xiao, *Nat. Energy* **2023**, *8*, 1273–1283; c) D. Wang, X. Zhu, X. Tu, X. Zhang, C. Chen, X. Wei, Y. Li, S. Wang, *Adv. Mater.* **2023**, *35*, e2304646; d) S. Jia, L. Wu, H. Liu, R. Wang, X. Sun, B. Han, *Angew. Chem. Int. Ed.* **2024**, e202400033; e) N. J. Harmon, J. Li, B. T. Wang, Y. Gao, H. Wang, *ACS Catal.* **2024**, *14*, 3575–3581; f) T. Xie, X. He, L. He, K. Dong, Y. Yao, Z. Cai, X. Liu, X. Fan, T. Li, D. Zheng, S. Sun, L. Li, W. Chu, A. Farouk, M. S. Hamdy, C. Xu, Q. Kong, X. Sun, *Chin. Chem. Lett.* **2024**, *35*, 110005; g) Y. Li, L. Quyang, J. Chen, X. Fan, H. Sun, X. He, D. Zheng, S. Sun, Y. Luo, Q. Liu, L. Li, W. Chu, J. Du, Q. Kong, B. Zheng, X. Sun, *J. Colloid Interface Sci.* **2024**, *663*, 405–412.

[11] a) P. Liao, J. Kang, R. Xiang, S. Wang, G. Li, *Angew. Chem. Int. Ed.* **2024**, *63*, e202311752; b) R. Zhao, Y. Wang, J. Fu, F. Zhang, L. Wen, Y. Zhao, B. Guan, B. Han, Z. Liu, *J. Am. Chem. Soc.* **2024**, *146*, 27956–27963; c) Y. Wu, Z. Jiang, Z. Lin, Y. Liang, H. Wang, *Nat. Sustain.* **2021**, *4*, 725–730.

[12] a) C. Tang, Y. Zheng, M. Jaroniec, S. Z. Qiao, *Angew. Chem. Int. Ed.* **2021**, *60*, 19572–19590; b) N. Li, C. Pan, G. Lu, H. Pan, Y. Han, K. Wang, P. Jin, Q. Liu, J. Jiang, *Adv. Mater.* **2023**, e2311023; c) D. Wang, X. F. Lu, D. Luan, X. W. Lou, *Adv. Mater.* **2024**, 2312645; d) R. Wu, Q. Meng, J. Yan, Z. Zhang, B. Chen, H. Liu, J. Tai, G. Zhang, J. Zhang, B. Han, *Nat. Catal.* **2024**, *7*, 702–718; e) P. Li, Q. Zhu, J. Liu, T. Wu, X. Song, Q. Meng, X. Kang, X. Sun, B. Han, *Chem. Sci.* **2024**, *15*, 3233; f) C. L. Rooney, H. Wang, *Nat. Synth.* **2024**, *3*, 792–793; g) M. Dan, X. Zhang, Y. Yang, J. Yang, F. Wu, S. Zhao, Z.-Q. Liu, *PNAS* **2024**, *121*, e2318174121.

[13] X. Zhang, H. Jing, S. Chen, B. Liu, L. Yu, J. Xiao, D. Deng, *Chem Catalysis* **2022**, *2*, 1807–1818.

[14] Y. Wu, W. Chen, Y. Jiang, Y. Xu, B. Zhou, L. Xu, C. Xie, M. Yang, M. Qiu, D. Wang, Q. Liu, Q. Liu, S. Wang, Y. Zou, *Angew. Chem. Int. Ed.* **2023**, *62*, e202305491.

[15] Y. Wu, J. Zhao, C. Wang, T. Li, B. H. Zhao, Z. Song, C. Liu, B. Zhang, *Nat. Commun.* **2023**, *14*, 3057.

[16] S. Jia, X. Tan, L. Wu, X. Ma, L. Zhang, J. Feng, L. Xu, X. Song, Q. Zhu, X. Kang, X. Sun, B. Han, *Chem. Sci.* **2023**, *14*, 13198–13204.

[17] a) J. Xian, S. Li, H. Su, P. Liao, S. Wang, R. Xiang, Y. Zhang, Q. Liu, G. Li, *Angew. Chem. Int. Ed.* **2023**, *62*, e202306726; b) J. Xian, S. Li, H. Su, P. Liao, S. Wang, Y. Zhang, W. Yang, J. Yang, Y. Sun, Y. Jia, Q. Liu, Q. Liu, G. Li, *Angew. Chem. Int. Ed.* **2023**, *62*, e202304007; c) R. Xiang, S. Wang, P. Liao, F. Xie, J. Kang, S. Li, J. Xian, L. Guo, G. Li, *Angew. Chem. Int. Ed.* **2023**, *62*, e202312239.

[18] a) B. H. Ko, B. Hasa, H. Shin, Y. Zhao, F. Jiao, *J. Am. Chem. Soc.* **2022**, *144*, 1258–1266; b) J. Liang, Z. Li, L. Zhang, X. He, Y. Luo, D. Zheng, Y. Wang, T. Li, H. Yan, B. Ying, S. Sun, Q. Liu, M. S. Hamdy, B. Tang, X. Sun, *Chem* **2023**, *9*, 1768–1827.

[19] M. Yasuda, N. Tsugita, K. Ito, S. Yamauchi, W. R. Glomm, I. Tsuji, H. Asano, *Environ. Sci. Technol.* **2011**, *45*, 1840–1846.

[20] a) S. Zhao, C. Tan, C.-T. He, P. An, F. Xie, S. Jiang, Y. Zhu, K.-H. Wu, B. Zhang, H. Li, J. Zhang, Y. Chen, S. Liu, J. Dong, Z. Tang, *Nat. Energy* **2020**, *5*, 881–890; b) H.-F. Wang, L. Chen, H. Pang, S. Kaskel, Q. Xu, *Chem. Soc. Rev.* **2020**, *49*, 1414–1448; c) X. Xiao, L. Zou, H. Pang, Q. Xu, *Chem. Soc. Rev.* **2020**, *49*, 301–331; d) C. Du, P. Li, Z. Zhuang, Z. Fang, S. He, L. Feng, W. Chen, *Coord. Chem. Rev.* **2022**, *466*, 214604; e) D.-W. Lim, H. Kitagawa, *Chem. Rev.* **2020**, *120*, 8416–8467; f) A. E. Khudozhitkov, N. Ogiwara, M. Donoshita, H. Kobayashi, A. G. Stepanov, D. I. Kolokolov, H. Kitagawa, *J. Am. Chem. Soc.* **2024**, *146*, 12950–12957; g) W. Wang, D. Chen, F. Li, X. Xiao, Q. Xu, *Chem* **2024**, *10*, 86–133.

[21] a) K. Y. Wang, J. Zhang, Y. C. Hsu, H. Lin, Z. Han, J. Pang, Z. Yang, R. R. Liang, W. Shi, H. C. Zhou, *Chem. Rev.* **2023**, *123*, 5347–5420; b) X. Zhang, C. Yang, P. An, C. Cui, Y. Ma, H. Liu, H. Wang, X. Yan, G. Li, Z. Tang, *Sci. Adv.* **2022**, *8*, eadd5678; c) J. Guo, Y. Qin, Y. Zhu, X. Zhang, C. Long, M. Zhao, Z. Tang, *Chem. Soc. Rev.* **2021**, *50*, 5366–5396; d) C. He, J. Liang, Y. H. Zou, J. D. Yi, Y. B. Huang, R. Cao, *Natl. Sci. Rev.* **2022**, *9*, nwab157; e) N. Behera, J. Duan, W. Jin, S. Kitagawa, *EnergyChem* **2021**, *3*, 100067; f) X. Peng, L. Chen, Y. Li, *J. Mol. Catal.* **2022**, *529*, 112568.

[22] a) J. P. Zhang, Y. B. Zhang, J. B. Lin, X. M. Chen, *Chem. Rev.* **2012**, *112*, 1001–1033; b) W. Cai, T. Lee, M. Lee, W. Cho, D. Y. Han, N. Choi, A. C. Yip, J. Choi, *J. Am. Chem. Soc.* **2014**, *136*, 7961–7971.

[23] a) V. Hosseininasab, J. A. Bertke, T. H. Warren, *Angew. Chem. Int. Ed.* **2021**, *60*, 21184–21188; b) C. J. Frederickson, J. Y. Koh, A. I. Bush, *Nat. Rev. Neurosci.* **2005**, *6*, 449–462; c) T. Miki, M. Awa, Y. Nishikawa, S. Kiyonaka, M. Wakabayashi, Y. Ishihama, I. Hamachi, *Nat. Methods* **2016**, *13*, 931–937;

d) Y. Z. Liu, H. Song, C. Zheng, S. L. You, *Nat. Synthesis* **2022**, *1*, 203–216.
[24] a) C. Li, H. Zhang, M. Liu, F.-F. Lang, J. Pang, X.-H. Bu, *Ind. Chem. Mater.* **2023**, *1*, 9–38; b) B. Xiao, P. S. Wheatley, X. Zhao, A. J. Fletcher, S. Fox, A. G. Rossi, I. L. Megson, L. Regli, K. M. Thomas, R. E. Morris, *J. Am. Chem. Soc.* **2007**, *129*, 1203–1209.
[25] a) M. A. Dheyab, A. A. Aziz, M. S. Jameel, O. A. Noqta, P. M. Khaniabadi, B. Mehrdel, *Sci. Rep.* **2020**, *10*, 10793; b) M. Li, Z. Zhu, S. Yuan, L. Ji, T. Zhao, Y. Gao, H. Wang, *J. Mol. Catal.* **2023**, *541*, 113076.
[26] Y. Qiao, N. He, X. Zhang, X. Zhao, X. Zhao, W. Li, C. Li, *New J. Chem.* **2022**, *46*, 14103–14111.
[27] a) A. C. Ferrari, J. Robertson, *Phys. Rev. B* **2000**, *61*, 14095; b) A. C. Ferrari, *Solid State Commun.* **2007**, *143*, 47–57.
[28] a) X. Wang, C. Zhao, B. Liu, S. Zhao, Y. Zhang, L. Qian, Z. Chen, J. Wang, X. Wang, Z. Chen, *Adv. Energy Mater.* **2022**, *12*, 2201960; b) X. Wu, H. Yue, Y. Zhang, X. Gao, X. Li, L. Wang, Y. Cao, M. Hou, H. An, L. Zhang, S. Li, J. Ma, H. Lin, Y. Fu, H. Gu, W. Lou, W. Wei, R. N. Zare, J. Ge, *Nat. Commun.* **2019**, *10*, 5165.
[29] J. H. Park, W. R. Lee, Y. Kim, H. J. Lee, D. W. Ryu, W. J. Phang, C. S. Hong, *Cryst. Growth Des.* **2014**, *14*, 699–704.
[30] M. Rafiee, M. N. Mayer, B. T. Punchihewa, M. R. Mumau, *J. Org. Chem.* **2021**, *86*, 15866–15874.
[31] D. Wang, N. He, L. Xiao, F. Dong, W. Chen, Y. Zhou, C. Chen, S. Wang, *Angew. Chem. Int. Ed.* **2021**, *60*, 24605–24611.
[32] K. S. Park, Z. Ni, A. P. Côté, J. Y. Choi, R. Huang, F. J. Uribe-Romo, H. K. Chae, M. O'Keeffe, O. M. Yaghi, *PNAS* **2006**, *103*, 10186–10191.
[33] a) C. Hennig, K. H. Hallmeier, G. Zahn, F. Tschwatschal, H. Hennig, *Inorg. Chem.* **1999**, *38*, 38–43; b) J. Hu, Q. Chen, H. Hu, X. Chen, F. Hu, Z. Yin, *Sep. Purif. Technol.* **2012**, *98*, 308–314; c) Q. Wang, T. Ina, W. T. Chen, L. Shang, F. Sun, S. Wei, D. Sun-Waterhouse, S. G. Telfer, T. Zhang, G. I. N. Waterhouse, *Sci. Bull.* **2020**, *65*, 1743–1751.
[34] a) M. Keilwerth, J. Hohenberger, F. W. Heinemann, J. Sutter, A. Scheurer, H. Fang, E. Bill, F. Neese, S. Ye, K. Meyer, *J. Am. Chem. Soc.* **2019**, *141*, 17217–17235; b) G.-X. Wang, X. Wang, Y. Jiang, W. Chen, C. Shan, P. Zhang, J. Wei, S. Ye, Z. Xi, *J. Am. Chem. Soc.* **2023**, *145*, 9746–9754; c) S. Shimomura, M. Higuchi, R. Matsuda, K. Yoneda, Y. Hijikata, Y. Kubota, Y. Mita, J. Kim, M. Takata, S. Kitagawa, *Nat. Chem.* **2010**, *2*, 633–637; d) M. Breedon, M. J. S. Spencer, I. Yarovsky, *Surf. Sci.* **2009**, *603*, 3389–3399; e) T. Zhao, J. Zhang, K. Li, Q. Xu, G. Lan, *Asian J. Chem.* **2014**, *26*, 5255–5258.
[35] a) W. Chen, Y. Wu, Y. Jiang, G. Yang, Y. Li, L. Xu, M. Yang, B. Wu, Y. Pan, Y. Xu, Q. Liu, C. Chen, F. Peng, S. Wang, Y. Zou, *J. Am. Chem. Soc.* **2024**, *146*, 6294–6306; b) S. Jia, L. Wu, X. Tan, J. Feng, X. Ma, L. Zhang, X. Song, L. Xu, Q. Zhu, X. Kang, B. Han, *J. Am. Chem. Soc.* **2024**, *146*, 10934–10942; c) Y. Wu, M. Li, T. Li, J. Zhao, Z. Song, B. Zhang, *Sci. China Chem.* **2023**, *66*, 1854–1859.
[36] a) Y. Wu, J. Zhao, C. Wang, T. Li, B.-H. Zhao, Z. Song, C. Liu, B. Zhang, *Nat. Commun.* **2023**, *14*, 3057; b) J. Wu, L. Xu, Z. Kong, K. Gu, Y. Lu, X. Wu, Y. Zou, S. Wang, *Angew. Chem. Int. Ed.* **2023**, *62*, e202311196.

Manuscript received: October 10, 2024
Version of record online: February 21, 2025